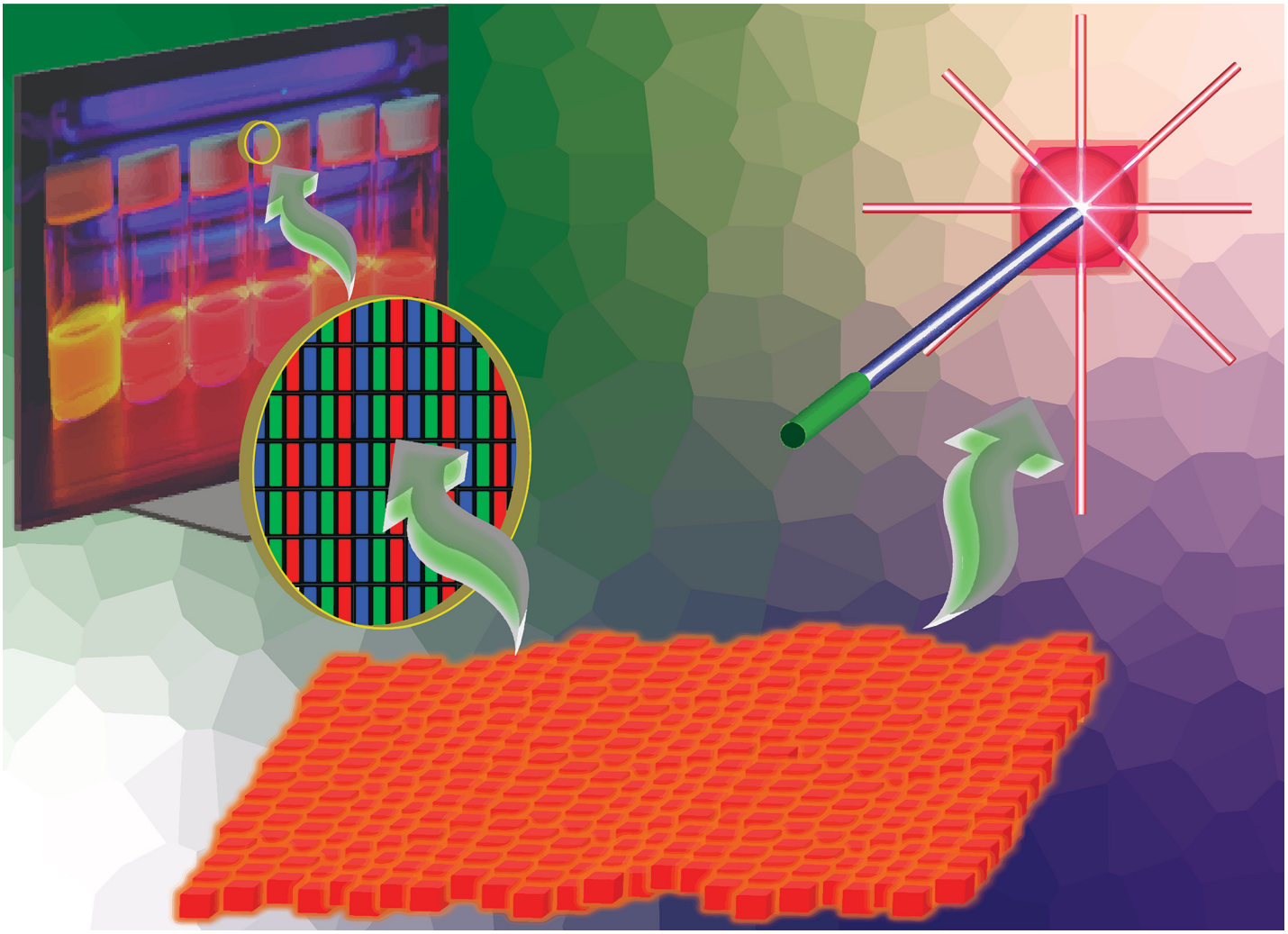

Showcasing collaborative research work from Department of Applied Chemistry and Institute of Molecular Science, Center for Emergent Functional Matter Science, National Yang Ming Chiao Tung University, and Department of Material Science and Engineering, National Tsing Hua University, Taiwan.

Functionalized hybrid perovskite nanocrystals with organic ligands showing a stable 3D/2D core/shell structure for display and laser applications

A perovskite nanocrystal film with a 4-trifluoromethyl-benzylammonium protection ligand exhibits a remarkable enduring stability with stabilized emission at 630 nm, which is suitable for display and laser applications.

As featured in:

See Eric Wei-Guang Diau *et al.*, *J. Mater. Chem. C*, 2021, **9**, 17341.

ROYAL SOCIETY OF CHEMISTRY

rsc.li/materials-c

Registered charity number: 207890

Journal of Materials Chemistry C

ROYAL SOCIETY OF CHEMISTRY

PAPER

View Article Online
View Journal | View Issue

Cite this: J. Mater. Chem. C, 2021, 9, 17341

Functionalized hybrid perovskite nanocrystals with organic ligands showing a stable 3D/2D core/shell structure for display and laser applications†

Sumit Shahajirao Bhosale,[a] Sudhakar Narra,[ab] Efat Jokar,[ab] Arumugam Manikandan,[c] Yu-Lun Chueh[c] and Eric Wei-Guang Diau *[ab]

A simple one-pot synthesis of stable red-emitting perovskite nanocrystals (PeNCs) involved the addition of Cs-oleate, formamidinium bromide (FABr) and organic ammonium iodide salts (represented as L*n*I, n = 1–5) to a hot flask containing oleic acid (OA), oleylamine (OLA) and PbI_2. The crystal structures of these PeNCs that are rich in halide on the surface enable surface-defect passivation, whereas they conform to structural formula $Cs_{1-x}FA_xPbBr_yI_{3-y}$ in the bulk. The photoluminescence (PL) spectrum of **L0** in the absence of L*n*I salts displays an orange colour at 589 nm, whereas those of **L1–L5** show red spectral shifts toward 622–629 nm in octane solutions. The PL decay profiles of these PeNCs (**L0–L5**) were fitted with a stretched-exponential function with lifetimes in the range of 11.1 (**L0**)–15.8 ns (**L3**) and with PL quantum yields 69 (**L5**)–79% (**L1**); the values of dispersion factor β are in the range of 0.91–0.94, indicating the diminished surface defects because of the rich halides on the surface. Upon storage of these thin-film samples in an ambient air environment with RH ~30%, the 3D/2D core–shell structure formed for **L1–L5** exhibited spectral shifts from ~640 nm toward smaller wavelengths. The PeNC film with a 4-trifluoromethyl-benzylammonium protection ligand (**L5**) exhibited a remarkable enduring stability with stabilized emission at 630 nm, which is suitable for display applications to serve as a red QD source. Using the femtosecond transient absorption spectral technique, we observed great optical gains for the **L5**/ethyl cellulose film, suitable for laser applications.

Received 27th August 2021,
Accepted 12th October 2021

DOI: 10.1039/d1tc04049a

rsc.li/materials-c

Introduction

Due to the rapid progress in the power conversion efficiency (PCE) of halide-perovskite solar cells, increasing from 3.8%[1] to 25.6%,[2] perovskite materials of general formula ABX_3 have received much attention for various purposes. Halide perovskites have many unique optical and electronic properties;[3] they are cost-effective *via* solution processing. Such halide perovskites have hence been broadly applied not only in photovoltaics[4] but also in areas of optoelectronics,[5,6] photocatalysis,[7,8] and so on. Thin-film perovskites suffer, however, from instability under ambient air conditions.[9] To stabilize halide perovskites, one efficient approach is to decrease the size of the perovskite structure to a nanometer scale to form perovskite nanocrystals (PeNCs).[9,10] These PeNCs demonstrate superior properties such as intense photoluminescence (PL), a tunable band gap and excellent stability.[11,12] Because of these unique properties, PeNCs are promising candidates for LED,[13] laser[14] and display applications.[15–18]

PeNCs can be synthesized by various methods, such as hot injection,[19] ligand-assisted reprecipitation[20] and top-down methods;[7] each method has its advantages and disadvantages.[11] Br-based PeNCs are typically green emitters[21] with a cubic crystal structure whereas their I-based counterparts are red emitters. The latter I-based PeNCs suffer from serious problems such as phase transition and chemical instability.[22] For instance, methylammonium lead triiodide ($MAPbI_3$) PeNCs are unstable because of the volatile nature of MA;[11] $CsPbI_3$ PeNCs suffer from a phase transition from the α-cubic phase (black phase) to the δ-orthorhombic phase (yellow phase).[22] Much effort has been exerted to stabilize the cubic phase of the $CsPbI_3$ PeNCs, such as reaction at high

[a] Department of Applied Chemistry and Institute of Molecular Science, National Yang Ming Chiao Tung University, 1001 Ta-Hsueh Rd, Hsinchu 30010, Taiwan
[b] Center for Emergent Functional Matter Science, National Yang Ming Chiao Tung University, 1001 Ta-Hsueh Rd, Hsinchu 30010, Taiwan. E-mail: diau@mail.nctu.edu.tw
[c] Department of Material Science and Engineering, National Tsing Hua University, Hsinchu, 30013, Taiwan

† Electronic supplementary information (ESI) available. See DOI: 10.1039/d1tc04049a

temperatures,[23] modulation of A-[24,25] and B-[26] site cations, bidentate ligand passivation,[27] chloride doping,[28] modification of the ligand shells and polymer encapsulation.[11] Another challenge of the red-emitting PeNCs is the tunability of the emission wavelength to a desired region (~630 nm) for display applications.[29] Although all specified strategies succeeded in stabilizing I-based PeNCs, most did not attempt to tune the wavelength of emission from 710 nm to 630 nm.[11] For the latter goal, post-treatments with bromide salts and B-site modifications have been reported.[24,30] Organic ammonium and metal–halide salts have been used as halide sources to passivate halide vacancies, but these reported synthetic methods are typically difficult to perform. For example, Yang *et al.*[31] used KBr to passivate PeNCs in which the potassium precursor was synthesized separately and trimethylsilyl iodide or bromide served as a halide source. Chiba *et al.*[32] and Imran *et al.*[33] used a post-treatment with quaternary salts and a benzyl halide, respectively, to improve the quality of nanocrystals. As an advance on the work of previous authors, we developed a simple and novel synthetic method to passivate the halide vacancies and concurrently to tune the emission wavelength.

Herein we report a novel one-pot synthetic approach, described as a hot-addition method (HAM), to synthesize hybrid PeNCs with their emission tuned to the desired red region, ~630 nm. Both the cation A site (Cs and formamidinium, FA) and the halide X site (Br and I) were modified to produce a general perovskite structure $Cs_{1-x}FA_xPbBr_yI_{3-y}$ with the photoluminescence quantum yield (PLQY) approaching 80%. As schematically shown in Fig. 1, in addition to oleic acid (OA) and oleylamine (OLA), one of five ammonium cations (represented as **L1–L5**; a sample with only OA and OLA ligands is represented as **L0**) to serve as protective ligands was added to protect the PeNCs in this approach without post-treatment. We selected ligands with a very short aliphatic chain (**L1**), short aliphatic chain (**L2**), cyclic aliphatic chain (**L3**), aromatic chain (**L4**), and fluorinated aromatic chain (**L5**) to study their interactions with PeNCs. These ammonium protection salts (L*n*I; n = 1–5) served to modify the ligand shell of PeNCs with L*n* cations to improve the stability and to tune the emission wavelength with iodine anions. The PL transients of all these ligand-modified PeNCs showed a nearly single-exponential decay feature, indicating slight contributions from surface defects. Upon storage, the ligand-modified PeNC thin films showed the formation of a 2D-shell structure on the surface of a 3D-core structure to protect the PeNCs from penetration of moisture; sample **L5** had stabilized emission at 630 nm suitable for red-emitting QD display applications. Furthermore, for film **L5**, the femtosecond transient absorption spectra (TAS) showed a great optical gain, appropriate for laser application.

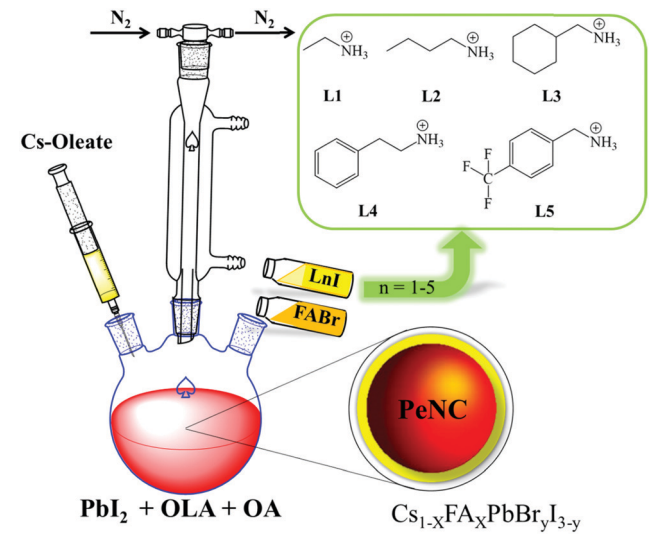

Fig. 1 Schematic representation of the hot-addition method to synthesize hybrid perovskite nanocrystals (PeNCs) $Cs_{1-x}FA_xPbBr_yI_{3-y}$ with protected ammonium cationic ligands L*n* for ethylammonium (**L1**), butylammonium (**L2**), cyclohexylmethylammonium (**L3**), phenylethylammonium (**L4**) and 4-trifluoromethyl-benzylammonium (**L5**). The precursor solution contained oleic acid (OA), oleylamine (OLA) and PbI_2 in 1-octadecene; caesium oleate (Cs-oleate), FABr and L*n*I were added separately at high temperatures.

Results and discusion

$CsPbI_3$ PeNCs have been previously reported to suffer from phase instability[22] due to the small ionic radius of Cs and the large ionic radius of I. For this reason, a FA cation and a Br anion were introduced to form a hybrid PeNC with an appropriate Goldschmidt tolerance factor and octahedral factor. This idea to use FABr to stabilize the PeNC phase of $CsPbI_3$ has been reported,[24] but the synthesis involved multiple steps with post-treatment of halides. In our HAM approach, we simplified the sequential reaction by introducing a hot addition of the FABr precursor and other protective organic ammonium ligands in a one-pot synthetic procedure to provide stabilization and passivation of surface defects of the hybrid PeNC.

In a traditional hot-injection method, $CsPbI_3$ PeNCs were produced on injection of Cs-oleate into a hot solution containing PbI_2, OLA and OA in 1-octadecene at high temperatures.[19] FABr in isopropyl alcohol (IPA) and the protective ligand L*n*I (n = 1–5) in IPA were added to the hot solution at flask temperatures of 140 and 150 °C, respectively; Cs-oleate was then injected at 200 °C and the flask was immediately immersed in an ice bath to complete the reaction. IPA is an appropriate solvent for the HAM because it not only dissolves organic cations but also acts as an antisolvent to form the hybrid PeNC.

Fig. 2 shows images from a transmission electron microscope (TEM); the sizes of particles are typically between 7 and 10 nm for all samples. These PeNCs show a uniform cubic shape similar to that previously reported.[34] According to the TEM analysis, the addition of ammonium salt does not affect the size distribution of PeNCs. High-resolution TEM images display a *d*-spacing that resembles that of the cubic phase of the perovskite with interplanar distances ~0.3 nm belonging to (200) and ~0.4 nm to (110). X-ray diffraction (XRD) patterns, shown in Fig. 3 feature two characteristic signals. Because of the small crystals of PeNCs, the XRD patterns show a broad diffraction feature covering characteristic signals of both cubic and orthorhombic phases of halide perovskites, which makes

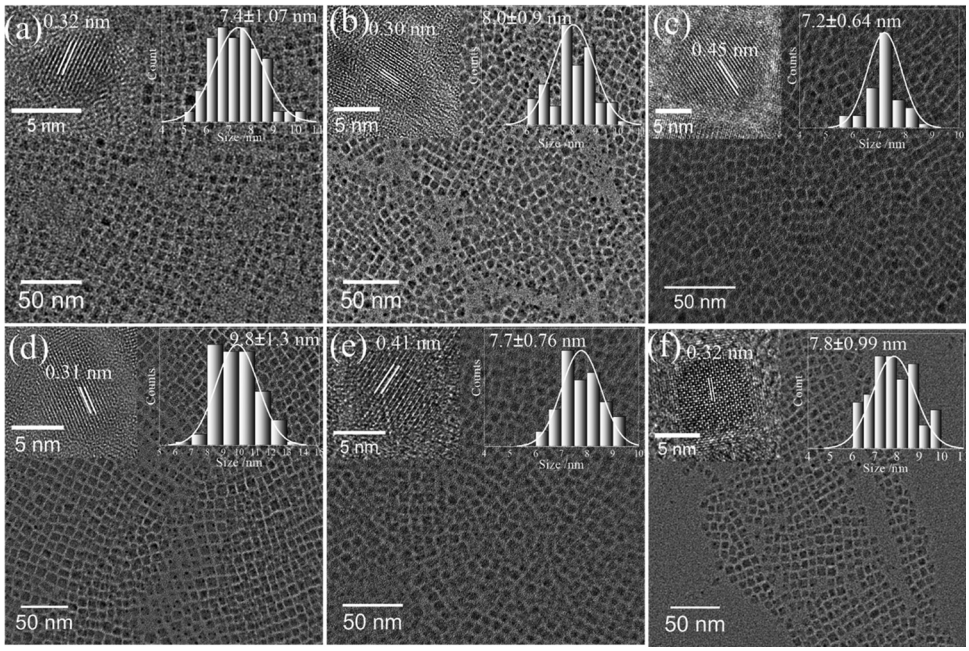

Fig. 2 TEM images of (a) **L0**, (b) **L1**, (c) **L2**, (d) **L3**, (e) **L4** and (f) **L5** used to plot the size distributions indicated in the insets of each plot. The insets show also the magnification of each nanocrystal labeling the *d*-spacing.

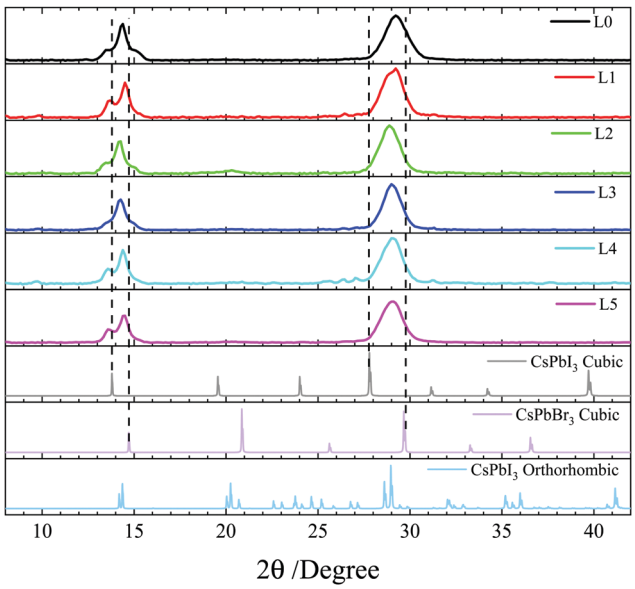

Fig. 3 X-ray diffraction patterns of thin-film PeNCs **L0–L5** fabricated with the drop-casting method. The XRD patterns of $CsPbBr_3$ and $CsPbI_3$ in various phases were obtained from the CIF database.[35–37]

assignments difficult for these XRD patterns.[35] The XRD signals at 2θ ~14.3° show satellite patterns due to the superlattice reflection.[36,37] The XRD patterns are similar for all PeNCs except that for **L0**, which is shifted to slightly larger angles because of a contribution of more bromide (less iodide) of **L0** without added L*n*I salts. A weak diffraction peak at 2θ ~9.8° corresponds to the 2D perovskite structures for the **L1** and **L4** samples. The similarity of the main XRD patterns for **L1–L5** indicates that these ammonium cations were not inserted inside the perovskite crystals, but they helped in modifying the ligand shells of the PeNC.

X-ray photoelectron spectra (XPS) shown in Fig. S1, ESI,† confirm the presence of the relevant elements such as Pb, Cs, Br and I in the perovskite structure. As XPS is sensitive to surfaces, surface-elemental composition was quantified by XPS (Table S1, ESI†). The results show that the Cs/Pb ratios were ~1 for **L1**, **L2** and **L4**, implying that no FA cations were involved on the surfaces of these PeNCs, but the proportions of FA on the surfaces of **L0**, **L3** and **L5** are estimated to be 0.06, 0.12 and 0.12, respectively. The ratio I : Br is larger for **L1–L5** than for **L0** because of the addition of L*n*I salts for the former. The ratio of halides (I + Br) to Pb on the surfaces of PeNCs was much greater than 3.0 for all samples, indicating that the surfaces of these ligand-modified PeNCs (**L0–L5**) were rich in halide. One reason for the latter feature on the surface might be the formation of a 2D-shell structure on the 3D-PeNC surface, in particular for the **L1** and **L4** samples with a greater (I + Br) : Pb ratio than the others. Energy-dispersive X-ray (EDX) analysis was performed to identify the elemental composition of bulk PeNCs; the corresponding EDX spectra are presented in Fig. S2 (ESI†), with results listed in Table S2 (ESI†). According to these results, the Cs : Pb ratio is less than 1.0 for all samples, implying that some part of Cs was replaced by FA cations (Table S2, ESI†). Differing from the XPS analysis, the EDX results show that the ratio of halides (I + Br) to Pb in the bulk is ~3 for **L3–L5**, which is consistent with the atomic ratio in the standard perovskite structure (ABX_3). In contrast, the ratio of halides (I + Br) to Pb is slightly greater than 3.0 for **L0–L2**, indicating that those PeNCs are slightly rich in halide in the bulk, but those ratios are significantly smaller than those on the surface. We hence

concluded that the crystal structures of these PeNCs are rich in halide on the surface (a 2D-shell might be involved) but in the bulk, they basically conform to structural formula $Cs_{1-x}FA_xPbBr_yI_{3-y}$.

We provide further evidence for the presence of ammonium cation ligands on the surfaces of PeNCs using the time-of flight secondary-ion mass-spectra (TOF-SIMS). Among all organic ammonium cations, only **L5** has fluorine atoms attached to the aromatic ring. The fluorine-ion signals were thus traced with TOF-SIMS to detect the presence of ammonium cations on the surface. Fig. S3 (ESI†) presents the ion images and mass spectra of fluorine for all PeNCs. **L5** clearly shows a much greater concentration of fluorine than other PeNCs because of the presence of the fluoro functional group of **L5** on the surface. Fluorine in trace proportions in other PeNCs arose from impurities in solvents or precursors during synthesis.

PeNCs synthesized with the HAM show exellent optical properties, presented in Fig. 4. In the insets of Fig. 4, the absorption spectrum of **L0** (Fig. 4a) in octane solution shows a large hypsochromic shift relative to other PeNCs **L1–L5**, due to a greater bromine content in **L0** than in other PeNCs. Accordingly, the PL spectrum of **L0** shows a maximum at 589 nm, whereas the ligand-modified PeNC shows PL maxima in the range of 622–629 nm, which is a suitable spectral characteristic for red emissive QDs for display applications.[29] The PL quantum yield (PLQY) was measured using a reference method, for which the standard was a solution of 4-(dicyanomethylene)-2-methyl-6-(4-dimethylaminostyryl)-4*H*-pyran (DCM) dye prepared in ethanol, which produces a PLQY of 43.7%.[38] The PLQY of all PeNCs are listed in Table S3 (ESI†). Even though the PL of **L0** is in the orange region, its PLQY attains 72%. The other red PeNCs also have excellent PLQYs, from 69% (**L5**) to 79% (**L1**).

Fig. 4 shows the PL-decay profiles of solution samples obtained from measurements using a time-correlated single-photon-counting (TCSPC) system with excitation at 375 nm and probed at the PL maximum for each PeNC in octane solution. The corresponding PL decays were fitted with a stretched-exponential-decay model according to this equation:

$$I_t = I_0 e^{\left[(-t/\tau)^{\beta}\right]}$$

Here τ is the decay-time coefficient and β is the dispersion factor ($0 \geq \beta \geq 1$).[39] Fig. S4 (ESI†) shows the fitted results and the corresponding residual plots for each decay. We found that a stretched-exponential function is better than a single-exponential decay function for the fit, as shown in the residual plots of Fig. S4 (ESI†). Here a stretched-exponential–decay curve was used to fit a non-single exponential decay, of which the β value represents the distribution of decay coefficients; a β value near unity corresponds to a narrow distribution of the decay coefficients.[40] According to the fitted results summarized in Table S4 (ESI†), the β values of the PeNCs are in the range of 0.91–0.94 for all samples, implying that all PL decays are dominated by the rate coefficient (k_r) for radiative recombination. The average PL lifetimes (τ_{PL}) are 11.1, 13.8, 14.3, 15.8, 14.2 and 14.4 ns for **L0–L5**, respectively; the surfaces modified with organic ammonium ligands (**L1–L5**) show greater PL lifetimes than that of the reference sample (**L0**).

The PL transients of nanomaterials generally show bi- or tri-exponential decay features, of which the first component is assigned to surface-defect recombination; the others are assigned to bulk recombination or bulk defects.[7,30] For the PeNC synthesized with our hot-addition method, the surface composition contains more halides than Pb. Based on previous

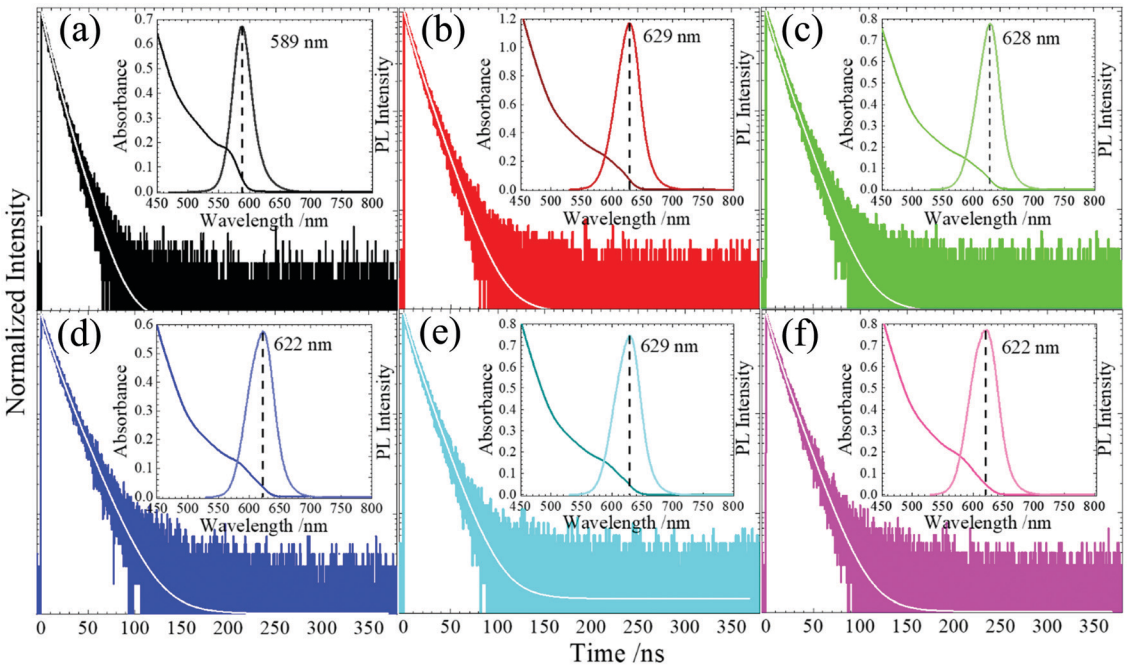

Fig. 4 PL decay profiles and absorption-emission spectra (insets) of (a) **L0** (b) **L1** (c) **L2** (d) **L3** (e) **L4** and (f) **L5** in octane solution.

reports, an increased proportion of Pb contained in the perovskite can affect the composition of the conduction band.[41] Perovskites are reported[3] to exhibit an inverted electronic structure compared to other typical III–V materials; the Pb 6s orbital is hence hybridized with the p orbital of a halide to form a valence band (VB) and the Pb 6p orbital is hybridized with the p orbital of the halide to form the conduction band (CB). The CB in the perovskite is dominated by Pb 6p; it is stabilized by spin–orbital splitting of the 6p orbital.[3] As the Pb contribution increases, the effect of spin–orbital splitting increases, which creates trapped states near the CB minima. An increased concentration of halides present on the surface suppresses the trap states and decreases the trap-assisted recombination so as to yield a nearly single-exponential decay ($\beta > 0.9$) of the PL, as we observed.

The stability of red-emitting PeNCs is the most challenging issue to be resolved; various strategies[20–24] have been applied to synthesize stable PeNCs for this purpose. Here we tested the stability of PeNCs **L0–L5** under two severe conditions. First, stability tests of the solution samples under ambient air conditions (RH = 60–70%) were performed to show a blue-shift spectral feature for all samples (Fig. S5, ESI†), indicating a release of iodide instead of bromide inside the perovskite structure in solution.[30] The samples were stable under ambient air conditions for more than one month, in particular for samples **L0** and **L5**. Second, stability tests of the PeNC films were performed under ambient conditions without encapsulation. Fig. S6a–c (ESI†) show the UV-vis and PL spectra, and XRD patterns of PeNC films stored under ambient air conditions (RH ~30%) for periods of storage up to 18 days. Upon storage, the UV-vis and PL spectra of **L1** to **L4** films showed a significantly blue-shifted spectral feature due to the loss of iodine from the structure, but **L0** and **L5** samples showed only a slight spectral change. The XRD patterns of the films presented in Fig. S6c (ESI†) demonstrate the crystal stability of the PeNCs. After storage for one week, the reactive PeNC surface sites formed by the detachment of OA and OLA react with the small ammonium cations (**L2** to **L5**) to produce a 2D shell. All ligand-modified PeNCs (**L1** to **L5**) showed a 2D-perovskite signal at a diffraction angle (2θ) slightly less than 10° (Fig. S6c, ESI†), indicating the formation of a 2D-structure on the surface of the PeNC to form a 3D/2D core–shell structure.[42] Although it is possible to form a separate 2D phase from the 3D structure, we did not observe any additional 2D signal in the PL spectra shown in Fig. S6b (ESI†). This 2D-shell is expected to have a protective effect on the 3D-core PeNC to enhance the stability, but, because of the release of the iodide species, the **L1–L4** PeNCs show degraded XRD patterns, similar to the UV-vis and PL spectra in Fig. S6a and b (ESI†). Because the PL spectra of these thin-film samples are red-shifted relative to those of the solution samples, the PL maximum of **L5** was originally located at 640 nm when the thin-film sample was freshly prepared, but shifted to 630 nm after storage for 7 days and remained at 630 nm for up to 18 days. The enhanced stability of the **L5** thin-film sample might be due to the fluorinated ligand present on the surface of PeNCs that prevents the collapse of the iodide component from the crystal structure and assists in forming a hydrophobic 2D-layer against the penetration of water.

The stability of the **L5** sample was confirmed on adding ethyl cellulose powder to the PeNC solution in toluene (ethyl cellulose, 10 mg, in PeNC solution, 1 mL). Ethyl cellulose aids in the formation of a homogeneous film without altering the optical properties of PeNCs and is capable of providing protection against moisture penetration. Fig. 5a and b show the UV-vis absorption and PL spectra of **L0** and **L5** samples, respectively. Through the synergistic effect of fluorinated ligand and ethyl cellulose, the **L5** film exhibited a remarkable

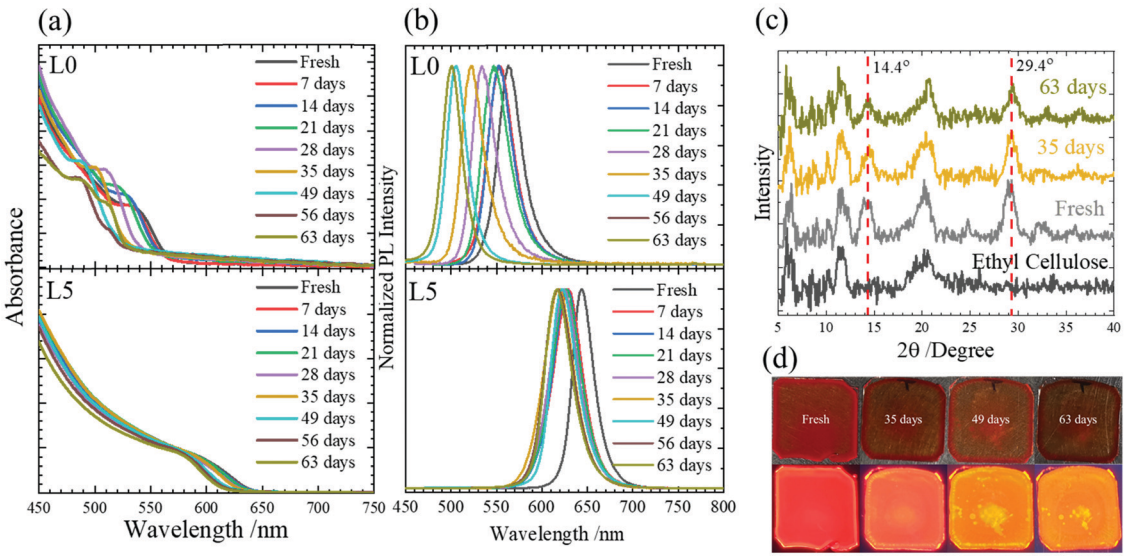

Fig. 5 Tests of stability of PeNCs (**L0** and **L5**) fabricated in ethyl-cellulose films without encapsulation showing (a) UV-vis and (b) PL spectra, and (c) XRD patterns under ambient air conditions (RH ~30%) for periods up to 63 days. (d) shows photographs of an **L5** sample at varied storage periods under irradiation with room light (top images) or UV light (375 nm; bottom images).

stability for over two months for the PL maximum shifted to ~620 nm. In contrast, the solid film of **L0** in ethyl cellulose shows instability due to the release of the iodide component upon storage. The XRD patterns of the **L5** sample (Fig. 5c) display no change in the crystal structure after storage for over two months (63 days). Fig. 5d further shows the photographs of the images of the **L5** film under irradiation. The Commission Internationale de l'Enclairage (CIE) coordinates of the **L5** sample were (0.67, 0.32) after storage for 14 days (Fig. S7, ESI†).[43] Our CIE and stability results thus confirm that the stabilized emission of the **L5** sample at 620–630 nm makes it a promising candidate for future display applications.

The exciton relaxation dynamics of the **L5** PeNC sample were investigated with femtosecond TAS with excitation at 640 nm and probe in the region of 500–740 nm. The thin-film samples were prepared using an ethyl cellulose host matrix of thickness 5 μm. The ground-state recovery dynamics of photogenerated excitons were monitored from the photobleach (PB) band minima at 615 nm (shown as an orange line in Fig. 6a), while the modulations associated with bandgap renormalization and band-broadening changes were monitored from the photoinduced absorption (PIA) band near 585 nm (shown as a green line in Fig. 5a). The strong PB band associated with a depletion of the excitonic state shows a rapid bandgap renormalization with band broadening shifted from the red to the blue region. The weak PIA band was assigned to changes of the refractive index in the film due to the generation of photoinduced excitons.[44] The PIA decay profile at 585 nm shown in Fig. 6b displays a tri-exponential decay feature with time coefficients 0.6 ps, 55 ps and ~ns. The two rapid-decay components might be assigned to rapid bandgap renormalization and slow band broadening, respectively. Alternatively, both sub-ps

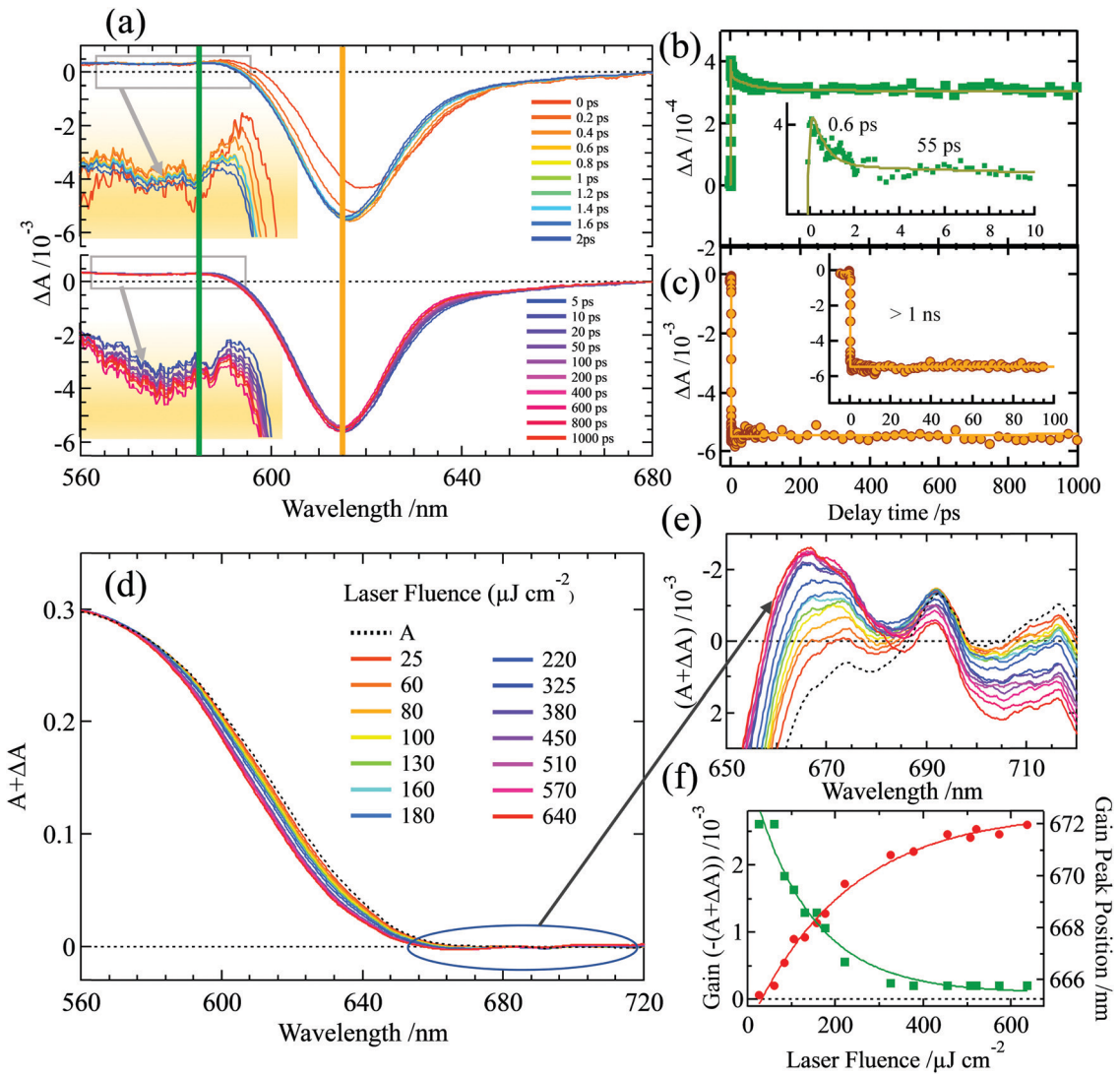

Fig. 6 (a) Femtosecond TA spectra of the **L5** sample with transient profiles monitored at (b) 585 nm (green line) and (c) 615 nm (orange line); (d) optical gain spectra with (e) sub-window showing enlarged gain magnitudes and (f) variations of gain peak position and gain magnitude as a function of laser fluence as indicated. The TA spectra (ΔA) were obtained on pumping the **L5** sample using a 640 nm laser pulse with a pulse energy 60 μJ cm^{-2} while the optical gain spectra ($A + \Delta A$) were obtained when the laser fluence was varied from 25 to 640 μJ cm^{-2} with excitation at 395 nm and probe delay 5 ps.

and ps components have small magnitudes; their origin could be either a rearrangement of halide ions following photoexcitation or a photoinduced structural change. The XRD signals of the PeNC samples are broad and show a close resemblance to both cubic and orthorhombic structures (Fig. 3). For this reason, it is also reasonable to assign the 0.6 ps component to a rapid rearrangement between the two crystal forms whereas the 55 ps component to halide-ion migration. In contrast, the bleach recovery at 615 nm shown in Fig. 6c displays only a step-function like response with a time scale ($\sim$ns) unresolvable using the current femtosecond TAS apparatus. The absence of sub-ps and ps components in the PB band indicates the suppression of biexcitons or ionized defects (trions) to the maximum extent in the measured **L5** PeNC sample.[45] This absence is consistent with the TCSPC result showing a PL lifetime of $\sim$14 ns with a nearly single exponential decay.

The optical-gain spectra (OGS) of the **L5** film were recorded on exciting the sample with a 70 fs pulse at 395 nm and probing in the visible region with a white-light continuum pulse generated from a sapphire crystal of thickness 3 mm.[46] The TA spectra were recorded at 5 ps following photoexcitation, at which delay the contributions due to hot excitons or band filling effects were diminished. To probe for the optical gain, we added the ΔA spectra measured at varied fluences from 25 to 640 μJ cm^{-2} to the steady-state absorption spectrum of the **L5** PeNC film as shown in Fig. 6d. As the laser power increased, the OGS showed an apparent blue-shifted feature in the PB region of the TA spectrum. The optical gain of the **L5** sample was observed in the sub bandgap region of the PB band (Fig. 6e) together with a blue spectral shift of the peak of the gain spectra toward the saturation region (Fig. 6f). The maximum optical gain was 2.5 $\times$ 10^{-3} at 666 nm with a laser gain threshold occurring at $\sim$32 μJ cm^{-2}, which is a promising photonic characteristic for its potential application as a red-colour laser.

Conclusion

We report here a one-pot method for the synthesis of stable red hybrid perovskite nanocrystals (PeNCs), $Cs_{1-x}FA_xPbBr_yI_{3-y}$, using a novel hot-addition method. Apart from oleic acid and oleylamine, the ligand shell of PeNCs was modified with five organic ammonium iodide salts – ethylammonium iodide (**L1**), butylammonium iodide (**L2**), cyclohexylmethylammonium iodide (**L3**), phenylethylammonium iodide (**L4**) and 4-trifluoromethyl-benzylammonium iodide (**L5**). In solution, the emission maximum of **L0** occurred at 589 nm, whereas the emission maxima of **L1–L5** were located at 622–629 nm with the PLQY in the range of 69–79%. These PeNCs have surfaces rich in halide that is responsible for defect passivation. The transient PL profiles were fitted with a stretched-exponential-decay model with β = 0.91–0.94, indicating that the hot addition method significantly suppressed both surface and bulk trap states. Furthermore, the formation of a 2D-perovskite structure on the surface of **L1–L5** PeNCs protects the 3D-core structure against the penetration of moisture, but releasing iodide instead of bromide leads to spectral shifts of the **L1–L4** samples toward smaller wavelength. With the protection of the fluorinated ligand, the **L5** thin-film sample exhibited a stabilized emission at 630 nm with excellent enduring stability. The stability duration of the **L5** PeNC film was further extended to over two months on blending **L5** PeNC solution with ethyl cellulose. Transient absorption spectra were recorded to investigate the exciton relaxation dynamics of **L5** PeNCs in an ethyl cellulose film. The TAS and TCSPC results unambiguously indicate that **L5** synthesized with the HAM has minimal surface and bulk defects. The optical gain of the **L5** sample was observed with the TAS technique at varied laser fluences, for which the power threshold of the optical gain was found to be as small as 32 μJ cm^{-2}. Our work thus reveals a new avenue for the development of red perovskite quantum-dot materials with great stability for promising future display and laser applications.

Conflicts of interest

There are no conflicts to declare.

Acknowledgements

Taiwan Ministry of Science and Technology (MOST 110-2123-M-A49-001 and MOST 110-2634-F-009-026) and Center for Emergent Functional Matter Science of National Yang Ming Chiao Tung University (NYCU) from The Featured Areas Research Center Program within the framework of the Higher Education Sprout Project by Taiwan Ministry of Education (MOE) supported this research.

References

1 A. Kojima, K. Teshima, Y. Shirai and T. Miyasaka, *J. Am. Chem. Soc.*, 2009, **131**, 6050–6051.
2 J. Jeong, M. Kim, J. Seo, H. Lu, P. Ahlawat, A. Mishra, Y. Yang, M. A. Hope, F. T. Eickemeyer, M. Kim, Y. J. Yoon, I. W. Choi, B. P. Darwich, S. J. Choi, Y. Jo, J. H. Lee, B. Walker, S. M. Zakeeruddin, L. Emsley, U. Rothlisberger, A. Hagfeldt, D. S. Kim, M. Grätzel and J. Y. Kim, *Nature*, 2021, **592**, 381–385.
3 J. S. Manser, J. A. Christians and P. V. Kamat, *Chem. Rev.*, 2016, **116**, 12956–13008.
4 R. Wang, M. Mujahid, Y. Duan, Z. Wang, J. Xue and Y. Yang, *Adv. Funct. Mater.*, 2019, **29**, 1808843.
5 Y.-C. Wang, H. Li, Y.-H. Hong, K.-B. Hong, F.-C. Chen, C.-H. Hsu, R.-K. Lee, C. Conti, T. S. Kao and T.-C. Lu, *ACS Nano*, 2019, **13**, 5421–5429.
6 K. Lin, J. Xing, L. N. Quan, F. P. G. de Arquer, X. Gong, J. Lu, L. Xie, W. Zhao, D. Zhang, C. Yan, W. Li, X. Liu, Y. Lu, J. Kirman, E. H. Sargent, Q. Xiong and Z. Wei, *Nature*, 2018, **562**, 245–248.
7 S. S. Bhosale, A. K. Kharade, E. Jokar, A. Fathi, S. M. Chang and E. W. G. Diau, *J. Am. Chem. Soc.*, 2019, **141**, 20434–20442.

8 Y. Wu, P. Wang, X. Zhu, Q. Zhang, Z. Wang, Y. Liu, G. Zou, Y. Dai, M.-H. Whangbo and B. Huang, *Adv. Mater.*, 2018, **30**, 1704342.
9 Y. Zhou and Y. Zhao, *Energy Environ. Sci.*, 2019, **12**, 1495–1511.
10 S. Paul and A. Samanta, *ACS Energy Lett.*, 2020, **5**, 64–69.
11 J. Shamsi, A. S. Urban, M. Imran, L. De Trizio and L. Manna, *Chem. Rev.*, 2019, **119**, 3296–3348.
12 S. Toso, D. Baranov and L. Manna, *Acc. Chem. Res.*, 2021, **54**, 498–508.
13 H.-C. Wang, Z. Bao, H.-Y. Tsai, A.-C. Tang and R.-S. Liu, *Small*, 2018, **14**, 1702433.
14 Q. Zhang, Q. Shang, R. Su, T. T. H. Do and Q. Xiong, *Nano Lett.*, 2021, **21**, 1903–1914.
15 J. Lin, Y. Lu, X. Li, F. Huang, C. Yang, M. Liu, N. Jiang and D. Chen, *ACS Energy Lett.*, 2021, **6**, 519–528.
16 F. Yan, S. T. Tan, X. Li and H. V. Demir, *Small*, 2019, **15**, 1902079.
17 M. V. Kovalenko, L. Protesescu and M. I. Bodnarchuk, *Science*, 2017, **358**, 745–750.
18 X. Wang, Z. Bao, Y.-C. Chang and R.-S. Liu, *ACS Energy Lett.*, 2020, **5**, 3374–3396.
19 L. Protesescu, S. Yakunin, M. I. Bodnarchuk, F. Krieg, R. Caputo, C. H. Hendon, R. X. Yang, A. Walsh and M. V. Kovalenko, *Nano Lett.*, 2015, **15**, 3692–3696.
20 L. C. Schmidt, A. Pertegás, S. González-Carrero, O. Malinkiewicz, S. Agouram, G. Mínguez Espallargas, H. J. Bolink, R. E. Galian and J. Pérez-Prieto, *J. Am. Chem. Soc.*, 2014, **136**, 850–853.
21 S. Rana, K. Awasthi, S. S. Bhosale, E. W.-G. Diau and N. Ohta, *J. Phys. Chem. C*, 2019, **123**, 19927–19937.
22 A. Dutta and N. Pradhan, *ACS Energy Lett.*, 2019, **4**, 709–719.
23 A. Dutta, S. K. Dutta, S. Das Adhikari and N. Pradhan, *Angew. Chem., Int. Ed.*, 2018, **57**, 9083–9087.
24 L. Protesescu, S. Yakunin, S. Kumar, J. Bär, F. Bertolotti, N. Masciocchi, A. Guagliardi, M. Grotevent, I. Shorubalko, M. I. Bodnarchuk, C.-J. Shih and M. V. Kovalenko, *ACS Nano*, 2017, **11**, 3119–3134.
25 M. Hao, Y. Bai, S. Zeiske, L. Ren, J. Liu, Y. Yuan, N. Zarrabi, N. Cheng, M. Ghasemi, P. Chen, M. Lyu, D. He, J. H. Yun, Y. Du, Y. Wang, S. Ding, A. Armin, P. Meredith, G. Liu, H. M. Cheng and L. Wang, *Nat. Energy*, 2020, **5**, 79–88.
26 S. Bera, D. Ghosh, A. Dutta, S. Bhattacharyya, S. Chakraborty and N. Pradhan, *ACS Energy Lett.*, 2019, **4**, 1364–1369.
27 J. Pan, Y. Shang, J. Yin, M. De Bastiani, W. Peng, I. Dursun, L. Sinatra, A. M. El-Zohry, M. N. Hedhili, A.-H. Emwas, O. F. Mohammed, Z. Ning and O. M. Bakr, *J. Am. Chem. Soc.*, 2018, **140**, 562–565.
28 S. Dastidar, D. A. Egger, L. Z. Tan, S. B. Cromer, A. D. Dillon, S. Liu, L. Kronik, A. M. Rappe and A. T. Fafarman, *Nano Lett.*, 2016, **16**, 3563–3570.
29 R. Zhu, Z. Luo, H. Chen, Y. Dong and S.-T. Wu, *Opt. Express*, 2015, **23**, 23680.
30 J. Zhang, L. Zhang, P. Cai, X. Xue, M. Wang, J. Zhang and G. Tu, *Nano Energy*, 2019, **62**, 434–441.
31 J.-N. Yang, Y. Song, J.-S. Yao, K.-H. Wang, J.-J. Wang, B.-S. Zhu, M.-M. Yao, S. U. Rahman, Y.-F. Lan, F.-J. Fan and H.-B. Yao, *J. Am. Chem. Soc.*, 2020, **142**, 2956–2967.
32 T. Chiba, Y. Takahashi, J. Sato, S. Ishikawa, H. Ebe, K. Tamura, S. Ohisa and J. Kido, *ACS Appl. Mater. Interfaces*, 2020, **12**, 45574–45581.
33 M. Imran, V. Caligiuri, M. Wang, L. Goldoni, M. Prato, R. Krahne, L. De Trizio and L. Manna, *J. Am. Chem. Soc.*, 2018, **140**, 2656–2664.
34 N. Pradhan, *ACS Energy Lett.*, 2021, **6**, 92–99.
35 W. J. Mir, A. Swarnkar and A. Nag, *Nanoscale*, 2019, **11**, 4278–4286.
36 S. Toso, D. Baranov, C. Giannini, S. Marras and L. Manna, *ACS Mater. Lett.*, 2019, **1**, 272–276.
37 M. C. Brennan, S. Toso, I. M. Pavlovetc, M. Zhukovskyi, S. Marras, M. Kuno, L. Manna and D. Baranov, *ACS Energy Lett.*, 2020, **5**, 1465–1473.
38 K. Rurack and M. Spieles, *Anal. Chem.*, 2011, **83**, 1232–1242.
39 J. Linnros, N. Lalic, A. Galeckas and V. Grivickas, *J. Appl. Phys.*, 1999, **86**, 6128–6134.
40 A. F. Van Driel, I. S. Nikolaev, P. Vergeer, P. Lodahl, D. Vanmaekelbergh and W. L. Vos, *Phys. Rev. B: Condens. Matter Mater. Phys.*, 2007, **75**, 1–8.
41 B. A. Koscher, J. K. Swabeck, N. D. Bronstein and A. P. Alivisatos, *J. Am. Chem. Soc.*, 2017, **139**, 6566–6569.
42 Y. Lin, Y. Bai, Y. Fang, Z. Chen, S. Yang, X. Zheng, S. Tang, Y. Liu, J. Zhao and J. Huang, *J. Phys. Chem. Lett.*, 2018, **9**, 654–658.
43 J. H. Heo, J. K. Park and S. H. Im, *Cell Rep. Phys. Sci.*, 2020, **1**, 100177.
44 D. Rossi, H. Wang, Y. Dong, T. Qiao, X. Qian and D. H. Son, *ACS Nano*, 2018, **12**(12), 12436–12443.
45 F. Liu, Y. Zhang, C. Ding, S. Kobayashi, T. Izuishi, N. Nakazawa, T. Toyoda, T. Ohta, S. Hayase, T. Minemoto, K. Yoshino, S. Dai and Q. Shen, *ACS Nano*, 2017, **11**(10), 10373–10383.
46 G. Yumoto, H. Tahara, T. Kawawaki, M. Saruyama, R. Sato, T. Teranishi and Y. Kanemitsu, *J. Phys. Chem. Lett.*, 2018, **9**(9), 2222–2228.

